

Effects of feedback on galaxies in the VELA simulations: elongation, clumps and compaction

Daniel Ceverino^{1,2*}, Nir Mandelker^{3,4}, Gregory F. Snyder⁵, Sharon Lapiner³,
Avishai Dekel^{3,6}, Joel Primack⁷, Omri Ginzburg³, Sean Larkin⁷

¹*Departamento de Física Teórica, Modulo 8, Facultad de Ciencias, Universidad Autónoma de Madrid, 28049 Madrid, Spain*

²*CIAFF, Facultad de Ciencias, Universidad Autónoma de Madrid, 28049 Madrid, Spain*

³*Centre for Astrophysics and Planetary Science, Racah Institute of Physics, The Hebrew University, Jerusalem 91904, Israel*

⁴*Kavli Institute for Theoretical Physics, Kohn Hall, Santa Barbara, CA 93106, USA*

⁵*Space Telescope Science Institute, 3700 San Martin Dr, Baltimore, MD 21218, USA*

⁶*SCIPP, University of California, Santa Cruz, CA 95064, USA*

⁷*Department of Physics, University of California, Santa Cruz, CA, 95064, USA*

Accepted XXX. Received YYY; in original form ZZZ

ABSTRACT

The evolution of star-forming galaxies at high redshifts is very sensitive to the strength and nature of stellar feedback. Using two sets of cosmological, zoom-in simulations from the VELA suite, we compare the effects of two different models of feedback: with and without kinetic feedback from the expansion of supernovae shells and stellar winds. At a fixed halo mass and redshift, the stellar mass is reduced by a factor of ~ 1 –3 in the models with stronger feedback, so the stellar-mass-halo-mass relation is in better agreement with abundance matching results. On the other hand, the three-dimensional shape of low-mass galaxies is elongated along a major axis in both models. At a fixed stellar mass, $M_* < 10^{10} M_\odot$, galaxies are more elongated in the strong-feedback case. More massive, star-forming discs with high surface densities form giant clumps. However, the population of round, compact, old (age_c > 300 Myr), quenched, stellar (or gas-poor) clumps is absent in the model with strong feedback. On the other hand, giant star-forming clumps with intermediate ages (age_c = 100 – 300 Myr) can survive for several disc dynamical times, independently of feedback strength. The evolution through compaction followed by quenching in the plane of central surface density and specific star-formation rate is similar under the two feedback models.

Key words: galaxies: evolution – galaxies: formation – galaxies: high-redshift

1 INTRODUCTION

Galaxies at high redshifts, $z \geq 1$, generate high levels of star formation, especially during the cosmic noon era, $z \approx 1 - 4$ (e.g., Whitaker et al. 2012; Madau & Dickinson 2014; Förster Schreiber & Wuyts 2020). The importance of stellar feedback from massive stars on galaxy-wide properties reaches a maximum during this epoch. The injection of energy, momentum, mass and metals has important consequences for the self-regulation of star formation (Dekel & Silk 1986; Governato et al. 2007; Ceverino et al. 2014; Hopkins et al. 2014; Agertz & Kravtsov 2015), galactic outflows (Oppenheimer & Davé 2008; Hopkins et al. 2012a; Muratov et al. 2015; Ceverino et al. 2016b), and metal enrichment inside and outside galaxies (Oppenheimer & Davé 2006; Ceverino et al. 2016a; Langan et al. 2020). Other important phenomena related to galaxy formation at high- z may also be sensitive to feedback: galaxy elongation (Ceverino et al. 2015, C15 hereafter), the formation and evolution of giant clumps within massive star-forming discs (Mandelker et al. 2017, M17 hereafter), and the compaction and quenching of com-

pact galaxies (Zolotov et al. 2015, Z15 hereafter). These processes are described below.

Observations that estimate the intrinsic shapes of the stellar components of high- z galaxies find that the distribution of projected axis ratios of high- z samples at $z = 1.5 - 4$ is inconsistent with a population of randomly oriented disc galaxies (Law et al. 2012; van der Wel et al. 2014; Zhang et al. 2019). They conclude that the intrinsic shapes of low-mass galaxies, $M_* < 10^{10} M_\odot$, are strongly triaxial. Therefore, galaxies evolve from triaxial to oblate as they build their stellar mass. This build-up is regulated by feedback. Therefore, this morphological transformation may depend on the feedback strength.

From the theoretical side, elongated galaxies are predicted within the current Λ cold dark matter (ACDM) paradigm (C15, Tomassetti et al. 2016; Meng et al. 2019; Pillepich et al. 2019). Triaxiality is a common property of dark matter (DM) halos in N-body-only simulations (Jing & Suto 2002; Allgood et al. 2006; Schneider et al. 2012, and references therein). A general result is that halos at a given mass scale are more prolate at earlier times. At the same time, the shape of the inner DM halo could influence the shape of the central galaxy (Dekel & Shlosman 1983) through the gravitational potential. If the galaxy is dominated by a non-axisymmetric, non-rotating potential, the stellar orbits are elongated along the major

* E-mail: daniel.ceverino@uam.es

axis of the triaxial halo (Binney & Tremaine 2008, sections 3.3.1 and 3.4.1). Therefore, the degree and evolution of elongation depend on the relative contribution of dark matter to the inner gravitational potential. This is related to the galactic stellar-to-DM fraction, which is sensitive to feedback.

A large fraction of massive, baryon-dominated galaxies at high- z are confirmed to be rotating but turbulent discs (Genzel et al. 2006; Förster Schreiber et al. 2009; Wisnioski et al. 2015). Many of these discs are broken into UV-bright giant clumps that each account for a few percent of the disc mass and at least 8% of the UV light (Elmegreen & Elmegreen 2005; Genzel et al. 2008; Guo et al. 2015, 2018). They are massive starburst regions, $M_* \simeq 10^7 - 10^9 M_\odot$, with stellar ages of around 100-200 Myr, consistent with recent episodes of star-formation (Wuyts et al. 2012). However observational estimates of the basic properties of clumps are still uncertain and they require a careful consideration of the systematic errors, using for example tools from machine learning (Huertas-Company et al. 2020; Ginzburg et al. 2021).

According to our understanding of high- z galaxy formation, these turbulent discs suffer violent disc instabilities (VDI), in which the strong inflow of cold gas (Dekel et al. 2009a) maintains high disc surface densities and marginally-unstable discs (Dekel et al. 2009b). In this scenario, the disc fragments into giant clumps around the Toomre mass scale (Toomre 1964; Inoue et al. 2016). This has been simulated in idealized conditions (Noguchi 1999; Bournaud & Elmegreen 2009; Hopkins et al. 2012b), and in cosmological simulations of galaxy formation (Agertz et al. 2009; Ceverino et al. 2010).

The lifetime of giant clumps is very sensitive to the strength and nature of stellar feedback. This has generated a debate about the final fate of these clumps. Simulations of moderate feedback have shown a population of clumps that live for many orbital periods, with lifetimes upto 1 Gyr (Ceverino et al. 2010; Mandelker et al. 2014, M17). On the other hand, simulations with stronger feedback disrupt clumps in much shorter times scales, 10-50 Myr (Genel et al. 2012; Oklopčić et al. 2017; Buck et al. 2017). These simulations use very different models of feedback, acting on different spatial and temporal scales. Therefore, their comparison is not straightforward.

VDI and clump migration account for about 25% of the total gas inflow to the galaxy center (Z15). The rest of the flow is coming from wet mergers and counter-rotating streams. If this inflow is much higher than the disc star-formation rate (SFR), this dissipative process leads to wet compaction (Dekel & Burkert 2014). This is a characteristic evolution pattern of high- z galaxies, composed by different phases (Z15). First, galaxies perturbed by gas-rich mergers, VDI or counter-rotating streams undergo a dissipative contraction into compact, star-forming galaxies (Barro et al. 2013) or massive bulges (Costantin et al. 2021). The increase of the stellar surface density within the inner 1-kpc radius, Σ_1 , occurs at a roughly time-independent specific SFR. Secondly, after compaction, there is a inside-out quenching of star formation into a compact, quiescent galaxy (Tacchella et al. 2016b). This is driven by a fast gas consumption and strong outflows and it occurs at constant Σ_1 . Finally, a long-term suppression of gas supply is needed to maintain quenching, through halo quenching (Birnboim & Dekel 2003) or AGN maintenance mode (Croton et al. 2006; Cattaneo et al. 2009; Fabian 2012). These processes are all sensitive to the strength and timescales of stellar feedback.

Stellar feedback is a mix of many different processes, from supernova explosions to radiation pressure. By adding new mechanisms, we can increase the strength of feedback and quantify its effect on the above processes of high- z galaxy formation: galaxy elongation, giant clumps, and compaction. In this numerical experiment, we are going

to compare two sets of cosmological simulations from the VELA suite with different models of feedback. This comparison can give us some insights about the trends with feedback strength.

Our first set of 35 simulated galaxies to be studied in detail was introduced in Ceverino et al. (2014) and Z15 and it is here renamed as VELA-3. The second set, dubbed VELA-6, includes the injection of momentum from the expansion of supernovae shells and stellar winds (Ceverino et al. 2017a). Section §2 summarises both models in detail. Section §3 describes the effect of feedback on the stellar-mass-halo-mass relation. Sections §4, §5 and §6 are devoted to galaxy elongation, clumps and compaction respectively. Finally, Section §7 ends with the summary and discussion.

2 SIMULATIONS

The VELA-3 and VELA-6 simulations use the same set of initial conditions. They only differ in their models of stellar feedback. These models have been developed from a pure thermal feedback model (VELA-2) with the addition of radiation pressure (VELA-3), photoheating/photoionization (VELA-4), and a moderate trapping of infrared photons (VELA-5). The last model, VELA-6, includes thermal, radiation pressure, moderate IR trapping and kinetic feedback. The comparison between VELA-2 and VELA-3 was discussed in Ceverino et al. (2014), Moody et al. (2014) and M17.

VELA-3 has been our standard set of simulations for several years. In addition to the works already mentioned, these simulations have been used to study metallicity inhomogeneities within galaxies (Ceverino et al. 2016a), the velocities of warm outflows (Ceverino et al. 2016b), and the link between halo and galaxy spin (Jiang et al. 2019), among other works that complement this paper. For example, VELA simulations help to distinguish between mergers and discs by simulating kinematic maps (Simons et al. 2019) and they also help to check the robustness of different dynamical mass estimates (Kretschmer et al. 2021). We learn how feedback regulates galaxy-wide star formation (Dekel et al. 2019), the mass threshold above which galactic discs may form (Dekel et al. 2020a), and the origin of star-forming rings (Dekel et al. 2020b). Finally, the connection between galaxy properties and the circumgalactic medium has been described in Roca-Fàbrega et al. (2019); Strawn et al. (2021). The comparison between VELA-3, VELA-4 and VELA-5 yields very similar results. Therefore, in this paper we are going to focus on the comparison between VELA-3 and VELA-6.

2.1 The Initial Conditions of VELA

VELA halos were drawn from N-body simulations with cosmological boxes of 10, 20 or 40 Mpc/h across, assuming a Λ CDM cosmology with $\Omega_m = 0.27$, $\Omega_\Lambda = 0.73$, $\Omega_b = 0.045$, $h = 0.7$ and $\sigma_8 = 0.82$. They were selected randomly in $\log M_{\text{vir}}$ in order to cover a halo mass range between $M_{\text{vir}} \sim 10^{11}$ and $\sim 10^{12} M_\odot$ at $z = 1 - 0.8$. Only ongoing major mergers at $z = 1$ were excluded. This only discarded 10% of the halos. In isolation, the median mass at $z = 0$ is about $10^{12} M_\odot$. However, the mass range is broad, with some of the halos merging into more massive halos hosting galaxy groups at $z = 0$ (Z15).

The selected halos were filled with gas and refined to a much higher resolution on an adaptive mesh within a zoom-in lagrangian volume that encompasses the mass within twice the virial radius (Klypin et al. 2002). The initial conditions of these runs contain between 6.4 to 46 $\times 10^6$ dark matter particles with a minimum mass of $8.3 \times 10^4 M_\odot$, while the particles representing single stellar populations that were

Table 1. Properties of the main progenitors in VELA-3 and VELA-6 simulations at $z = 2$ and z_{last} , the last available redshift. The unit for virial radius, R_v is proper kpc. Virial masses, M_{vir} , have units of $10^{12} M_{\odot}$ and stellar masses, M_* , have units of $10^{10} M_{\odot}$. The stellar mass is defined using all stars within a sphere of $0.1 R_v$. At a fixed halo mass and redshift, the stellar mass is reduced by a factor of ~ 1 -3 in models with stronger feedback.

Run	z_{last}	VELA-3						VELA-6						
		R_v	M_{vir}	M_*	$R_v(z=2)$	$M_{\text{vir}}(z=2)$	$M_*(z=2)$	z_{last}	R_v	M_{vir}	M_*	$R_v(z=2)$	$M_{\text{vir}}(z=2)$	$M_*(z=2)$
V01	1	124	0.48	1.5	58	0.16	0.2	1	122	0.46	0.79	57	0.15	0.057
V02	1	115	0.39	0.95	55	0.13	0.16	1	113	0.37	0.70	54	0.13	0.067
V03	1	108	0.32	1.0	56	0.13	0.38	1	108	0.32	0.49	55	0.13	0.10
V04	1	90	0.18	0.35	53	0.12	0.082	1	88	0.17	0.14	53	0.12	0.046
V05	1	83	0.14	0.27	44	0.070	0.072	1	83	0.15	0.095	43	0.063	0.032
V06	1.7	109	0.74	2.6	88	0.54	2.1	1	200	1.9	4.4	93	0.63	0.81
V07	1.5	145	1.4	7.3	104	0.89	5.7	1.5	150	1.5	7.4	107	0.97	4.6
V08	0.9	182	1.3	4.4	71	0.28	0.35	0.9	183	1.3	2.9	71	0.28	0.11
V09	1.5	121	0.83	4.3	71	0.28	1.0	0.8	209	1.7	5.1	64	0.21	0.50
V10	0.8	159	0.76	3.4	55	0.13	0.60	0.8	182	1.14	1.7	55	0.13	0.37
V11	0.8	106	0.37	1.6	70	0.27	0.76	0.8	158	0.74	0.73	68	0.25	0.37
V12	1.5	86	0.29	2.1	69	0.26	1.9	0.8	159	0.76	2.8	76	0.35	1.5
V13	1.5	108	0.59	2.2	73	0.30	0.57	0.8	169	0.92	3.5	72	0.29	0.30
V14	1.8	86	0.39	2.3	76	0.36	1.3	0.8	145	0.58	2.3	76	0.34	0.47
V15	0.8	123	0.35	1.5	53	0.12	0.51	0.8	125	0.37	0.52	53	0.12	0.18
V16	3.2	63	0.50	4.1	-	-	-	2.3	84	0.62	3.6	-	-	-
V17	2.2	106	1.1	8.4	-	-	-	2.2	108	1.2	4.7	-	-	-
V18	-	-	-	-	-	-	-	2.2	79	4.8	2.2	-	-	-
V19	2.4	91	0.87	4.4	-	-	-	2.3	96	0.92	4.1	-	-	-
V20	1.3	146	1.1	7.5	87	0.53	3.5	1.3	148	1.1	5.6	101	0.82	4.0
V21	1	151	0.88	6.5	92	0.62	4.0	1	156	0.98	5.7	94	0.65	3.3
V22	1	136	0.63	4.6	85	0.50	4.4	1	150	0.86	4.4	88	0.54	3.4
V23	1	123	0.47	2.5	57	0.15	0.76	1	122	0.46	1.4	57	0.15	0.47
V24	1.1	108	0.36	2.1	70	0.28	0.87	1	117	0.41	1.5	69	0.27	0.65
V25	1	108	0.32	1.4	65	0.22	0.68	1	107	0.31	0.62	68	0.25	0.19
V26	1	120	0.44	2.2	77	0.36	1.6	1	120	0.44	1.6	76	0.35	1.1
V27	1	114	0.38	2.0	75	0.34	0.71	1	114	0.37	1.3	75	0.34	0.48
V28	1	96	0.22	0.49	63	0.20	0.18	1	94	0.21	0.30	63	0.20	0.082
V29	1	152	0.90	0.37	84	0.52	0.20	1	153	0.91	3.2	87	0.52	1.8
V30	1.9	76	0.32	1.6	73	0.31	1.6	1.8	80	0.34	1.2	73	0.32	1.1
V31	4.3	38	0.22	0.8	-	-	-	1.8	117	1.1	4.1	105	0.93	3.8
V32	2	90	0.6	2.7	90	0.6	2.7	2	101	0.82	2.2	101	0.82	2.2
V33	1.6	144	1.5	9.4	101	0.83	4.8	1.5	148	1.5	6.9	107	0.98	2.5
V34	1.8	97	0.62	1.9	86	0.34	0.76	2.4	66	0.34	0.32	-	-	-
V35	3.5	37	0.14	0.49	-	-	-	3	48	0.2	0.23	-	-	-

formed in the simulation have a minimum mass of $10^3 M_{\odot}$. Each AMR cell is split into eight cells once it contains a mass in stars and dark matter higher than $2.6 \times 10^5 M_{\odot}$, equivalent to three dark matter particles, or once it contains a gas mass higher than $1.5 \times 10^6 M_{\odot}$. This quasi-Lagrangian strategy ends at the highest level of refinement that marks the minimum cell size at each redshift. This size is between 17-35 proper pc. More details can be found in Ceverino et al. (2014) and Zolotov et al. (2015).

2.2 ART

The ART code (Kravtsov et al. 1997; Kravtsov 2003) accurately follows the evolution of a gravitating N-body system and the Eulerian gas dynamics using an AMR approach. Besides gravity and hydrodynamics, the code incorporates many of the astrophysical processes relevant for galaxy formation. These processes, representing sub-grid physics, include gas cooling due to atomic hydrogen, helium, molecular hydrogen and metals down to a minimum temperature of 300 K. The code also includes a pressure floor to prevent artificial fragmentation (Ceverino et al. 2010). Other relevant processes are

photoionisation heating by a constant cosmological UV background with partial self-shielding, star formation and feedback, as described in Ceverino & Klypin (2009), Ceverino et al. (2010), and Ceverino et al. (2014).

2.3 Thermal Feedback

The model of thermal feedback assumes that each stellar particle acts as a single stellar population and injects their mechanical luminosity from supernovae and stellar winds as thermal heating, injected into the cell that host the stellar particle. The model assumes a constant heating rate over 40 Myr, following the values from STARBURST99 (Leitherer et al. 1999). More details and discussions can be found in Ceverino & Klypin (2009).

2.4 Radiative Feedback

In addition to thermal-energy feedback, the simulations use radiative feedback (Ceverino et al. 2014). This model adds a radiation pressure to the total gas pressure in regions where ionising photons from

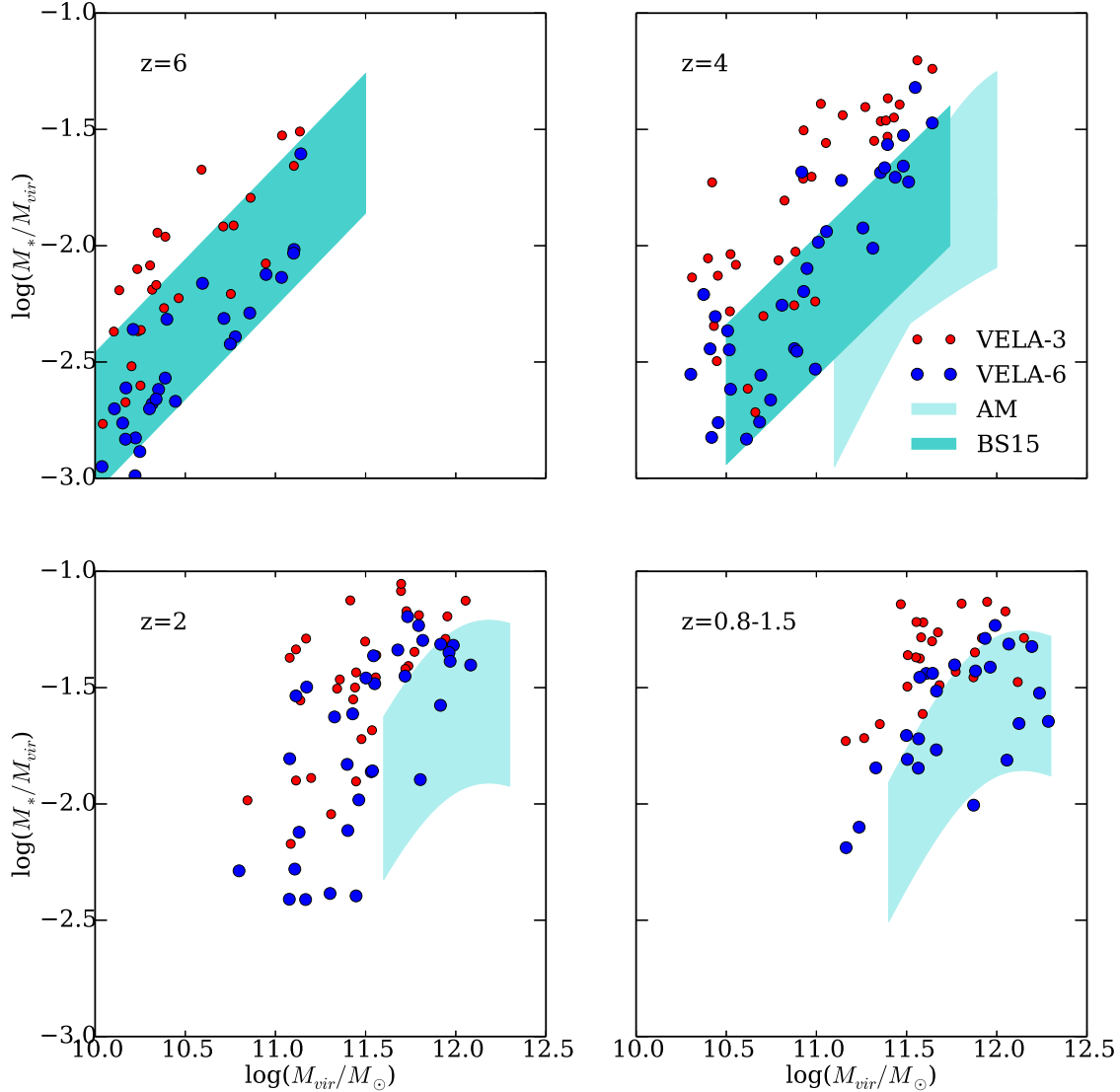


Figure 1. Ratio between stellar mass and virial mass at different redshifts. At the same virial mass, VELA-6 (blue) have a factor $\sim 1\text{--}3$ lower stellar mass than VELA-3 (red), in better agreement with the results from abundance matching (AM: [Moster et al. 2013](#); [Behroozi et al. 2013](#); [Rodríguez-Puebla et al. 2017](#); [Moster et al. 2018](#); [Behroozi et al. 2019](#)) and other empirical models at high redshift (BS15: [Behroozi & Silk 2015](#)).

massive stars are produced and trapped. In the model used in VELA-3, named RadPre in [Ceverino et al. \(2014\)](#), radiation pressure is included in the cells (and their closest neighbours within a sphere of radius equal to the cell size) that contain stellar particles younger than 5 Myr and whose gas column density exceeds 10^{21} cm^{-2} . Instead, VELA-6 uses the model RadPre_IR. In addition to the effect of ionising photons, the model adds a moderate trapping of infrared photons, only if the gas density in the host cell exceeds a threshold of 300 cm^{-3} . In this simple model, we assume that the optical depth of infrared photons scales linearly with the gas density, regardless of gas metallicity or dust composition. More details and discussion can be found in [Ceverino et al. \(2014\)](#).

2.5 Kinetic feedback

In addition to radiative feedback, VELA-6 also includes the injection of momentum coming from the (unresolved) expansion of gaseous shells from supernovae and stellar winds ([Ostriker & Shetty 2011](#)), as described in [Ceverino et al. \(2017b\)](#). A momentum of $10^6 M_{\odot} \text{ km s}^{-1}$ per massive star (i.e. per star more massive than $8 M_{\odot}$) is injected at a constant rate over 40 Myr, the lifetime of the lightest star that explodes as a core-collapsed supernovae. The model also takes into account a factor 3 boost in the injected momentum due to the clustering of supernovae ([Gentry et al. 2017](#)). The injection of momentum is

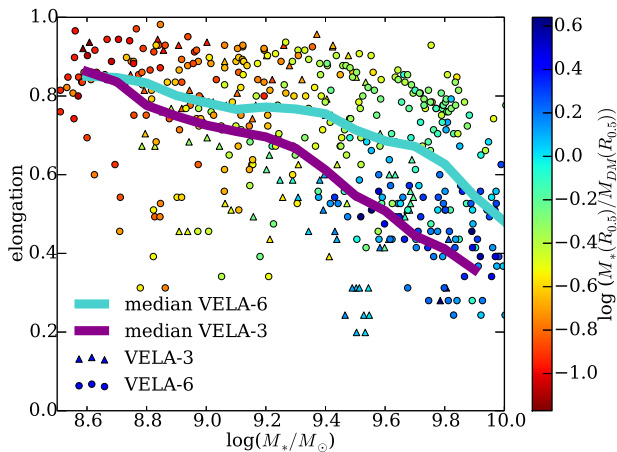


Figure 2. Elongation parameter (eq. 1) versus stellar mass for all available snapshots of VELA-3 and VELA-6 at $z = 1 - 3$, color coded by the star-to-DM mass ratio within the half-mass radius. The median values (solid lines) show that the elongation decreases with increasing mass and mass ratio but the trend is weaker for VELA-6. Galaxies in models with stronger feedback are more elongated. More massive galaxies ($M_* > 10^{10} M_\odot$) are not shown as they are preferentially axisymmetric.

implemented in the form of a non-thermal pressure, as described in Ceverino et al. (2017b).

This model differs from other recent implementations of kinetic feedback. It goes beyond the thermal-only feedback (Stinson et al. 2013; Schaye et al. 2015), and it does not shut down cooling in the star-forming regions (Stinson et al. 2006). It does not impose a wind solution (Hopkins et al. 2014; Vogelsberger et al. 2014), so that outflows are generated in a self-consistent way (Ceverino et al. 2016b). Our implementation is more similar to the feedback model in (Agertz & Kravtsov 2015).

3 STELLAR-MASS-HALO-MASS RELATION

One of the main effects of feedback is the self-regulation of the galaxy formation efficiency (Ceverino et al. 2014; Hopkins et al. 2014, and references therein). That efficiency can be quantified by the stellar-mass-halo-mass (SMHM) relation. The halo mass is measured as the virial mass (Bryan & Norman 1998) and the stellar mass is computed within 10% of the virial radius. Table 1 shows these properties at $z = 2$ and at the last available snapshot for VELA-3 and VELA-6 respectively. Figure 1 shows the SMHM ratio at different redshifts. In general, that ratio decreases towards low masses, as stellar feedback regulates star formation. There is a large scatter of about a factor 2 around the average ratio, driven by the different mass accretion histories (Moster et al. 2018). At a fixed halo mass, VELA-6 halos have a factor $\sim 1-3$ lower stellar mass than in VELA-3, due to their stronger feedback. The biggest difference is concentrated at low masses, $M_{\text{vir}} \leq 10^{11} M_\odot$, where stellar feedback is most efficient (Dekel & Silk 1986).

VELA-6 galaxies agree better with available results from models of abundance matching (Moster et al. 2013; Behroozi et al. 2013; Rodríguez-Puebla et al. 2017; Moster et al. 2018; Behroozi et al. 2019), and other empirical models at high redshifts (Behroozi & Silk 2015; Tacchella et al. 2018). We added an uncertainty of a factor 2 in these models that takes into account systematic differences due to

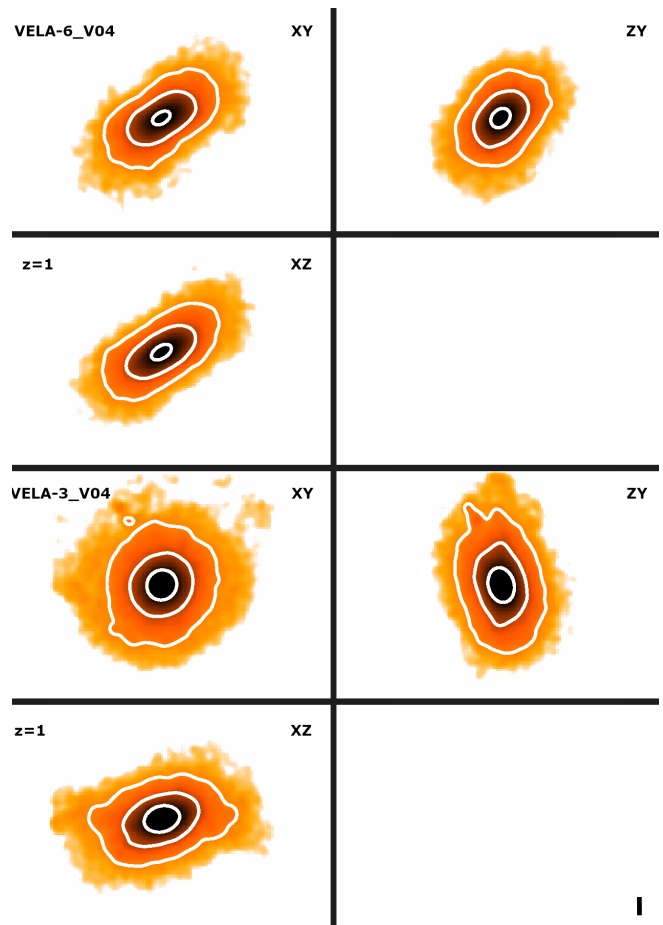


Figure 3. Three orthogonal projections (XY, XZ and ZY) of the stellar surface density of the same galaxy (V04) in the VELA-6 (top two panels) and VELA-3 (bottom two panels) at $z = 1$. Contours show isodensities of 4, 20 and $100 M_\odot \text{pc}^{-2}$. The bar in the bottom-right corner marks 1 kpc. VELA-6 galaxies are significantly more elongated, $a > b$, than the VELA-3 counterparts.

different cosmology and IMF assumptions, as well as uncertainties in the stellar mass estimates (Leja et al. 2019).

VELA-6 also agrees with the FirstLight simulations at $z \simeq 6$ (Ceverino et al. 2017b), which use a similar feedback model but have twice better spatial resolution. These overall results seem numerically converged to the extent to which we are able to test. They are still sensitive to feedback. Only future simulations will tell us whether we have reached model-independent values.

4 ELONGATION

The degree of intrinsic, 3D elongation of a galaxy can be quantified by the elongation parameter, as defined in C15,

$$e = \sqrt{1 - (b/a)^2} \quad (1)$$

where a and b are the major and intermediate axes of a 3D ellipsoidal shell that fits the stellar iso-density surface at the galaxy 3D half-mass radius, $R_{0.5} \simeq a$, as described in C15. In short, the calculation starts by computing the stellar density at the point of each stellar particle by using a 80-particle kernel. A first guess of the major axis direction at a radius $R_{0.5}$ uses the eigenvectors of the inertia tensor computed from

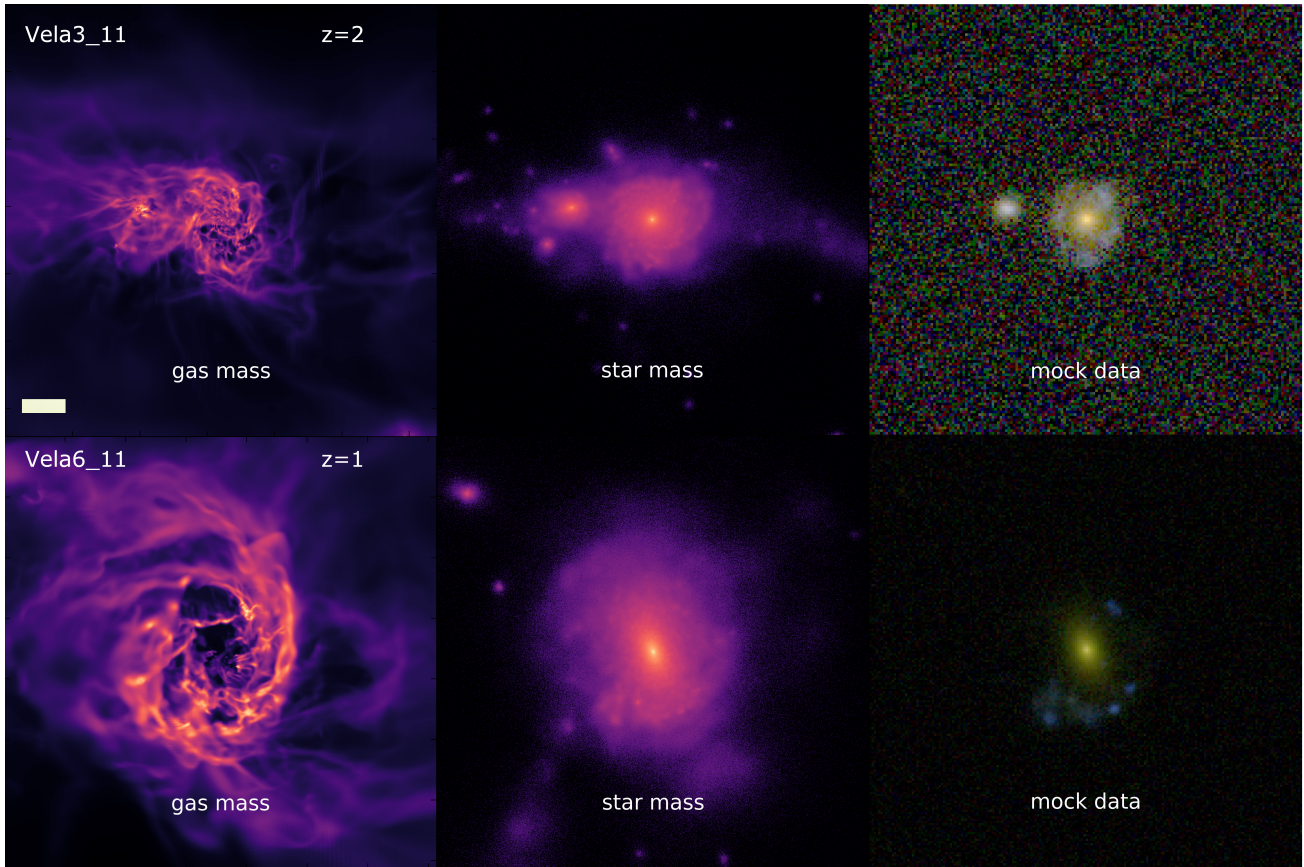


Figure 4. Two examples of face-on views of the same galaxy (V11) in VELA-3 (top) and VELA-6 (bottom) datasets with the same stellar mass, $M_* \approx 6 \times 10^9 M_\odot$, but at two different redshifts. The VELA-3 example shows a small axisymmetric disc while the VELA-6 case shows an elongated galaxy surrounded by a star-forming ring. The size of the images is 100 kpc. The scale bar marks 10 kpc. The mock HST images (right) are roughly rest-frame U-B-V bands.

all stars within a spherical shell at that radius. Then, the isodensity surface is defined by all particles with assigned density similar to the density at $R_{0.5}$ in the direction of the major axis. Finally, an ellipsoidal fit to that isodensity surface defines the main axes: a , b and c .

Figure 2 shows elongation versus galaxy mass, coloured by the stellar-to-DM mass ratio within $R_{0.5}$. The results of VELA-3 were obtained in C15. These simulations show that a galaxy achieves a high elongation if DM mass dominates over stellar mass within the galaxy. In this case, the elongation of the DM halo dominates the gravitational potential, which sets the galaxy elongation. As galaxy mass and halo mass increases, the stellar fraction increases and the galaxy elongation decreases. This is because baryons make rounder halos (Zemp et al. 2012), especially in the inner parts, where baryons dominate the potential. VELA-6 shows a weaker trend between elongation and mass, because star formation is less efficient at a fixed halo mass.

At a fixed stellar mass, the mass fraction in DM is higher in VELA-6. Therefore, they are more DM dominated and more elongated than VELA-3. That difference is more striking for masses between $10^{9.5}$ and $10^{10} M_\odot$, where galaxies are preferentially more elongated in VELA-6 than in VELA-3, independently of the actual value of the elongation parameter.

Figure 3 shows stellar mass projections of the same galaxy (V04) at $z = 1$ in both suites. The XY projection coincides with the face-on view of the galaxy, according to the angular momentum of the cold gas. The VELA-6 case shows a typical elongated galaxy ($e = 0.7$) of

low stellar mass, $M_* = 1.4 \times 10^9 M_\odot$. It is DM dominated within $R_{0.5}$, $M_*(R_{0.5})/M_{\text{DM}}(R_{0.5}) = 0.25$. This is similar to the case shown in C15. The VELA-3 example is more massive, $M_* = 3.5 \times 10^9 M_\odot$, and it shows a more oblate shape ($a \approx b$), typical of a massive, baryon-dominated galaxy with $M_*(R_{0.5})/M_{\text{DM}}(R_{0.5}) = 1.2$.

Figure 4 compares the same galaxy in the two datasets (V11) but now the galaxy mass is the same, $M_* \approx 6.5 \times 10^9 M_\odot$. Therefore, the selected snapshots have different redshifts. Both galaxies have roughly the same luminosity but the VELA-6 case lives in a halo that is twice more massive, $M_{\text{vir}} = 5.6 \times 10^{11} M_\odot$, than in the VELA-3 example. This drives a big difference in their stellar-to-DM mass fraction within $R_{0.5}$. The VELA-6 case is DM-dominated, $M_*(R_{0.5})/M_{\text{DM}}(R_{0.5}) = 0.5$, while the contribution of baryons is much more relevant in the VELA-3 example ($M_*(R_{0.5})/M_{\text{DM}}(R_{0.5}) = 1$).

The galaxy in VELA-3 shows an oblate axisymmetric disc, as also shown in Tomassetti et al. (2016). This is seen both in the stellar maps as well as in the mock HST image, obtained with SUNRISE as described in Simons et al. (2019) and Snyder et al. (2015). The VELA-6 case is far from axisymmetry ($e = 0.8$ at $R_{0.5} \approx 3$ kpc). The mock data in rest-frame U-B-V bands shows an elongated galaxy surrounded by a clumpy star-forming ring. The rest-frame visible bands follow the elongated stellar shape while the rest-frame UV traces the star-forming gas clumps of the gaseous disc.

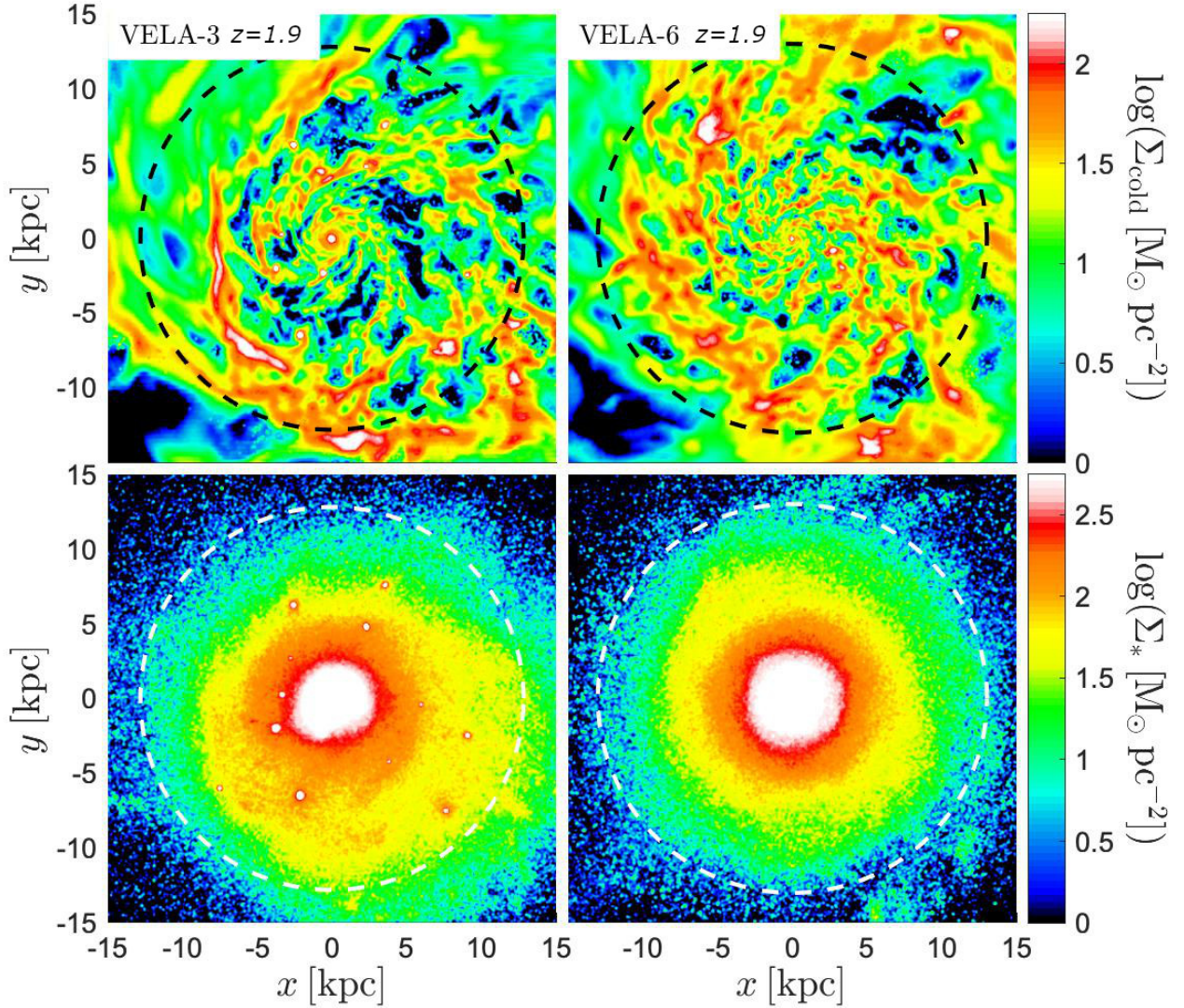


Figure 5. Face-on views of cold gas plus young stars, $T < 1.5 \times 10^4$ K and age < 100 Myr (top) and all stars (bottom) of V07 at $z \approx 2$ for VELA-3 (left) and VELA-6 (right). Circles represent the disc radius as defined in M17. Clumps in VELA-3 are significantly denser and rounder. Gas is clumpy in both models but dense clumps are absent in the stellar map of VELA-6.

5 CLUMPS

Massive, $M_{*} \geq 10^{10} M_{\odot}$, galaxies develop a thick rotating disk, which undergoes violent disk instability (Dekel et al. 2009b; Ceverino et al. 2010) and the formation of giant in-situ clumps (Mandelker et al. 2014, M17). We have used the clump finder described in M17 to generate catalogs of clumps in VELA-3 and VELA-6. The finder uses a cloud-in-cell interpolation to deposit mass from star particles and cold ($T < 1.5 \times 10^4$ K) gas cells into a uniform 3D grid with a cell size of $\Delta = 70$ pc. For each component, it applies a gaussian filter to smooth the density field and it calculates a density residual in each point, $\delta_{\rho} = (\rho - \rho_w)/\rho_w$, where ρ and ρ_w are the original and smoothed fields. Finally, it takes the maximum of the two residual values (stars or gas) at each point. We define clumps as connected regions containing at least 8 grid cells above a residual threshold,

$\delta_{\rho}^{\text{min}} = 10$. More details and a discussion of the sensitivity of results to parameter variations can be found in M17. The final clump catalog contains the properties of regions with stellar and/or gas densities that are at least 10 times higher than their local surroundings.

5.1 Examples of clumpy galaxies

Figure 5 shows a massive, $M_{*} > 10^{10} M_{\odot}$, baryon-dominated galaxy in the two datasets. The distribution of cold gas plus young stars ($T < 1.5 \times 10^4$ K, age < 100 Myr) looks clumpy in both cases. However, in VELA-3 there is a population of small and compact clumps that is absent in VELA-6. The clumps with stronger feedback look more irregular and elongated. The stellar distribution clearly shows dense and round stellar overdensities in VELA-3. The stellar

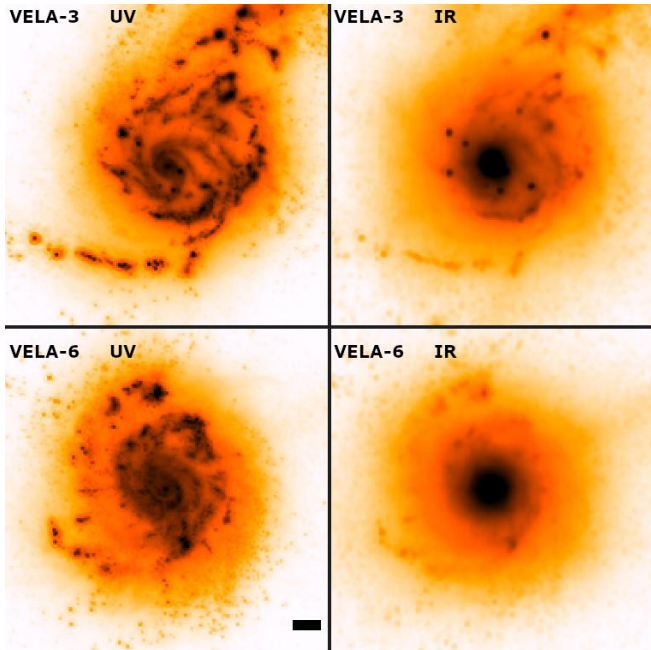


Figure 6. Mock images in the HST F606W band (left) and JWST F277W band (right) for VELA-3 (top) and VELA-6 (bottom) of the same galaxy from Figure 5, assuming a Milky-Way-like dust model. The bar marks 5 kpc. The rest-frame UV is clumpy in both models. However, the rest-frame near-IR is significantly less clumpy in models with stronger feedback.

disc in VELA-6, where feedback is stronger, is significantly less clumpy and the stellar clumps are less prominent.

Young stars (and indirectly the star-forming gas) can be traced by rest-frame UV, while the near-IR traces stellar mass. Figure 6 shows mock images of the same typical $z \approx 2$ galaxy shown in Figure 5. They are performed using Sunrise. We created high resolution mock images for both the VELA-3 and VELA-6 simulations using the Sunrise dust radiative transfer code (Jonsson 2006; Jonsson et al. 2010). They are a follow up to earlier generations of VELA mock images presented by Snyder et al. (2015) and Simons et al. (2019), now publicly available in the Mikulski Archive for Space Telescopes (MAST)¹. These mock images include face-on, edge-on, and random viewing orientations. We used the STARBURST99 stellar population models (Leitherer et al. 1999) with a Milky-Way-like dust model or an SMC-like dust model. We created images using a variety of HST, JWST, and Roman broadband imaging filters, which make them suitable for comparing with observations. We plan to submit these new mock images to MAST. Figure 6 uses the HST F606W filter for the rest-frame UV and the JWST F277W band for the rest-frame near-IR image. The HST image looks clumpy in both datasets. Clumps show a large variety of sizes and shapes. They all trace the same dense, star-forming regions seen in Figure 5. The JWST images look very different. In particular, bright and round clumps in VELA-3 are absent in VELA-6. Only some clumps associated with large star-forming regions can be barely seen above the disc background. Therefore, the rest-frame near-IR looks less clumpy than the rest-frame UV in models with strong feedback. This is consistent with the trends seen in other simulations (Buck et al. 2017) and in observations. Images in the rest-frame optical bands look less

clumpy than the UV counterparts (Wuyts et al. 2012; White et al. 2022). JWST’s larger diameter will allow better resolution of clumps than HST. Our results suggest that JWST observations that provide rest-frame near-IR images of galaxies at $z \approx 2$ will be crucial for mapping the stellar distribution of clumpy galaxies and they will be able to distinguish between different feedback scenarios.

5.2 Clump statistics

We analyzed clump properties following the methods described in M17. The clump mass, M_c , is the total baryonic mass (stars and gas) within the clump volume. The clump radius, R_c , is defined as the radius of a sphere with the same volume as the clump. The shape of this volume is characterized by its inertia tensor. We define the shape parameter as $S_c = I_3/I_1$, where I_1 and I_3 are the largest and the smallest eigenvalues of the tensor. A perfect sphere yields $S_c = 1$ and a flattened oblate clump has $S_c \approx 0.5$.

Clumps are tracked through time in the simulations using their stellar particles. While tracking the clump throughout its lifetime, we use the same definition of clump time, t , as used in M17. This is the time since the clump formation. When a given clump is identified for the first time, we compute t as the stellar age of the clump if this is lower than the time since the previous snapshot. Otherwise, we set $t = 0$. If a clump is identified at later snapshots, we increase t by the corresponding time interval. $t_{c,\max}$ is the clump time at the last snapshot of the clump. We refer to M17 for further details. We only follow in-situ clumps that formed within the central galaxies. Ex-situ clumps are small galaxies that joined the disc through mergers. They are excluded based on their dark matter content or the birth place of their stellar particles.

Figure 7 shows the mass-radius plane of clumps, as in Figure 6 from M17, for VELA-3 and VELA-6 in-situ clumps. The maps are coloured by the shape parameter, S_c and the clump age, t , normalized by the disc dynamical time, t_d . At low clump masses, the distribution of clumps is similar in both cases. This regime is dominated by clumps with $t_{c,\max} = 0$, defined as zero-lifetime clumps (ZLC) in M17. They are mostly transient features in the density field. At higher masses, $M_c > 10^7 M_\odot$, the clumps in VELA-6 have lower baryonic densities in general, as a result of a stronger feedback.

The distribution of clump shapes is very similar, with the exception of round clumps, $S_c \geq 0.7$. They are not present in the runs with strong feedback, as seen in Figures 5 and 6. The only oblate clumps with $S_c \approx 0.4 - 0.6$ seen in VELA-6 correspond to the densest clumps that survive feedback. These can retain a coherent structure in Jeans equilibrium between self-gravity, shear and feedback (Dekel et al. 2022b,a).

Figure 7 shows the distribution of clump age at a given snapshot with respect to the disc dynamical time. In both datasets, there is a large fraction of transient clumps with very short ages. These clumps are quickly disrupted due to feedback right after the onset of star formation. Most of them are ZLC as described in M17. This population is also seen in other simulations with strong feedback (Genel et al. 2012; Oklopčić et al. 2017) with lifetimes between 10-50 Myr, much shorter than the disc dynamical time.

A second population of clumps has ages longer than the disc dynamical time. These clumps can migrate within the disc and can drive gas inflows towards the galaxy centre (Dekel et al. 2009b; Ceverino et al. 2010, M17). However, the properties of the migrating clumps differ in the two datasets. Migrating clumps in VELA-6 are rarer and denser than in VELA-3. They usually have $\Sigma_{\text{bar}} \geq 400 M_\odot \text{pc}^{-2}$ and $V_{\text{circ}} \geq 40 \text{ km s}^{-1}$ in VELA-6, whereas migrating clumps in VELA-3 have $\Sigma_{\text{bar}} \geq 200 M_\odot \text{pc}^{-2}$ and $V_{\text{circ}} \geq 20 \text{ km s}^{-1}$.

¹ See <https://archive.stsci.edu/prepds/vela/>

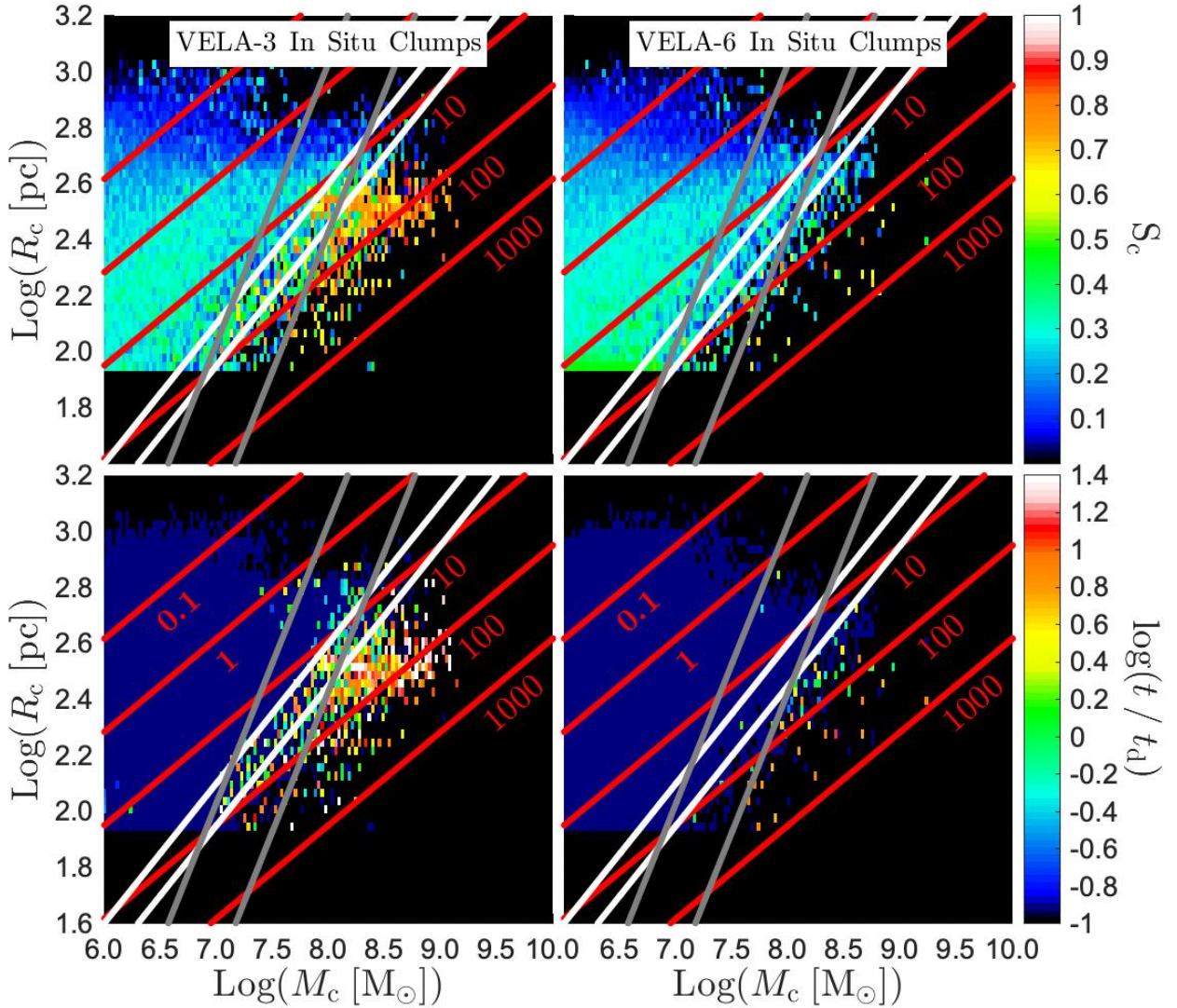


Figure 7. Distribution of clumps in the mass-radius plane for VELA-3 (left) and VELA-6 (right). Top panels are coloured by the shape parameter, S_c and bottom panels show the clump age in units of the disc dynamical time. Clumps with $t = 0$ were artificially set to dark blue. The red lines represent constant baryonic density in units of cm^{-3} . The grey lines represent a constant circular velocity of $V_{\text{circ}} = 20$ and 40 km s^{-1} , while white lines represent a constant baryonic column density of $\Sigma_{\text{bar}} = 200$ and $400 M_{\odot} \text{pc}^{-2}$. VELA-6 clumps are significantly less round. In VELA-3, migrating clumps with times longer than the disc dynamical time have typically $V_{\text{circ}} > 20 \text{ km s}^{-1}$ and $\Sigma_{\text{bar}} > 200 M_{\odot} \text{pc}^{-2}$. The stronger feedback in VELA-6 pushes migrating clumps to higher values: $V_{\text{circ}} > 40 \text{ km s}^{-1}$ and $\Sigma_{\text{bar}} > 400 M_{\odot} \text{pc}^{-2}$.

It seems that migrating clumps should be denser in order to survive stronger feedback. With respect to ages, VELA-6 migrating clumps have shorter ages, $t \leq 10 t_d$, whereas the range of ages in VELA-3 is much broader, $t = (1 - 30)t_d$. A more detailed analysis of clump evolution is discussed in a companion paper (Dekel et al. 2022b,a).

As discussed in M17, VELA-3 runs show a bimodality in clump lifetimes, $t_{c,\text{max}}$ with respect to their free-fall times, t_{ff} . We keep the same nomenclature and use the same threshold, $20t_{\text{ff}}$, to distinguish between short-lived clumps (SLCs) and long-lived clumps (LLCs), after excluding all ZLCs from further analysis ($t_{c,\text{max}}=0$). In VELA-6, that bimodal distribution is absent (Figure 8) and LLCs only

account for an extended tail in the distribution of clump lifetimes. This is consistent with the results from isolated disc simulations with strong feedback (Hopkins et al. 2012b). Therefore, the fraction of LLC in VELA-6 is much lower than in VELA-3. Feedback is limiting the lifetime of clumps but it also decreases the average clump densities, increasing the clump free-fall times.

The clump mass function (Figure 8) is very similar among the two models if clump masses are normalised by the disc mass, defined as all cold gas plus stars with high angular momentum within the galaxy radius (M14). SLCs dominate by number in both cases. Only the distribution of LLCs is radically different. LLCs with low masses,

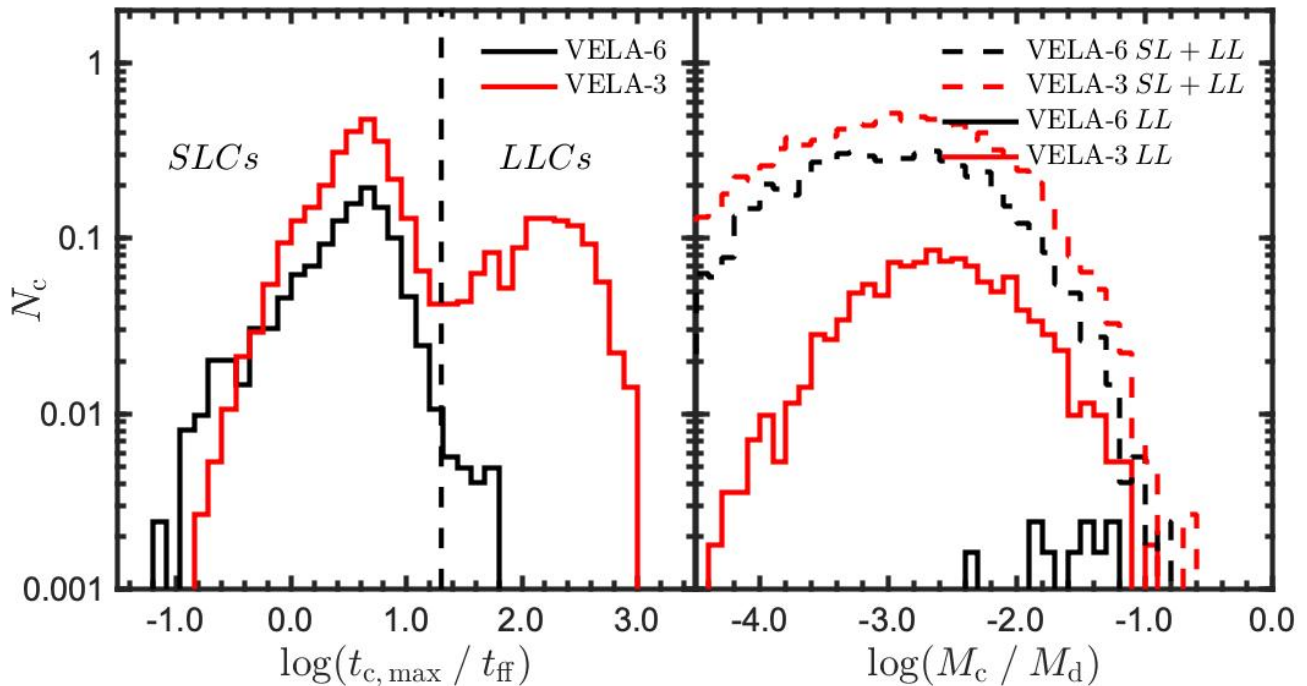


Figure 8. Distributions of clump lifetimes, $t_{c,\max}$, normalized to the mass-weighted clump free-fall time (left) and clump masses, normalized to the disc mass (right). Zero-lifetime clumps are excluded. The number of long-lived clumps with lifetimes longer than 20 free-fall times (vertical dashed line) is drastically reduced in VELA-6. They are limited to the most massive clumps with masses similar to the Toomre mass, $\log(M_c/M_d) \approx -1.5$.

$M_c/M_d \leq 0.03$, dominate the LLCs population in VELA-3. That population disappears in VELA-6. The rarer LLCs in VELA-6 are limited to the most massive clumps ($M_c/M_d \geq 0.03$) with masses similar to the Toomre mass. These giant clumps are massive enough to survive feedback, as steady winds generated by feedback are not expected to unbind them (Krumholz & Dekel 2010).

5.3 Gradients

Figure 9 compares various clump properties as a function of their cylindrical distance from the galaxy center, referred to as clump gradients, for in-situ clumps in VELA-3 and VELA-6. This is analogous to Figure 15 in M17. The gradients of SLCs in VELA-3 and VELA-6 are relatively similar. They show a steep age gradient with typical clump ages of 100-200 Myr. They are gas-rich, with higher sSFR and lower metallicities than the disc. The only difference is that SLC gradients in VELA-6 show slightly lower sSFR, higher gas fraction, and lower metallicity than the corresponding SLC gradients in VELA-3. The increase in feedback strength produces a decrease in the star-formation efficiency within these clumps.

LLCs show very different gradients. The population of old (age_c > 300 Myr), gas poor ($f_{\text{gas},c} < 0.1$) LLCs with sSFR lower than the underlying disc and high metallicity is absent in VELA-6. In particular, a population of quenched clumps ($\log(\text{sSFR}_c/\text{sSFR}_d) < -3$, where subscripts c and d refer to clump and disk), which accounts for 40% of the total population of LLCs in VELA-3 (M17) have disappeared in VELA-6. Feedback may prevent the formation of these stellar-rich clumps. As a result, typical ages in VELA-6 clumps extend to 100-300 Myr, consistent with observations (Wuyts et al. 2012; Guo et al. 2015). A more detailed comparison with observations requires the use of mock observations (Huertas-Company et al. 2020; Ginzburg et al. 2021) and this will be the focus of future work.

In VELA-6, there are no clumps at low galactocentric distances, $d < 0.2R_d$. It seems that clumps in models with stronger feedback are disrupted before they reach the galaxy centre, delivering gas and stars into the inner 20% of the disc radius. Clump evolution and its contribution to the growth of the bulge will be discussed in follow-up papers.

6 COMPACTION AND QUENCHING

Gas inflows within galactic discs, partially driven by migrating clumps and minor mergers, naturally trigger wet compaction and inside-out quenching (Dekel & Burkert 2014; Zolotov et al. 2015; Tacchella et al. 2016a). Figure 10 shows an example of compaction and quenching in VELA-3 and VELA-6. The overall behaviour is similar in both models. At high redshifts, the galaxy is star-forming and diffuse (pre-compaction phase), characterized by a relatively high sSFR and low surface stellar density in the inner 1 kpc, Σ_1 . After some time, the galaxy reaches a maximum in Σ_1 . This marks the compaction event. The sSFR remains high during the peak of compaction. After that maximum, the galaxy reduces its sSFR (quenching) and enters into the post-compaction phase with roughly constant Σ_1 within a factor of 2. This path in the Σ_1 -sSFR plane, also seen in observations (Barro et al. 2013), seems robust against variations in the feedback strength. The only noticeable difference is that compaction happens a little earlier in VELA-3 and the maximum density is higher. Most probably this is due to a higher stellar production in VELA-3.

The evolution of the mass in the different components within the central 1 kpc is a key feature in compaction events (Figure 11). In the VELA-3 run, the peak in gas and SFR within 1 kpc is narrower in time than in VELA-6. The maximum gas mass is also a factor 2 lower

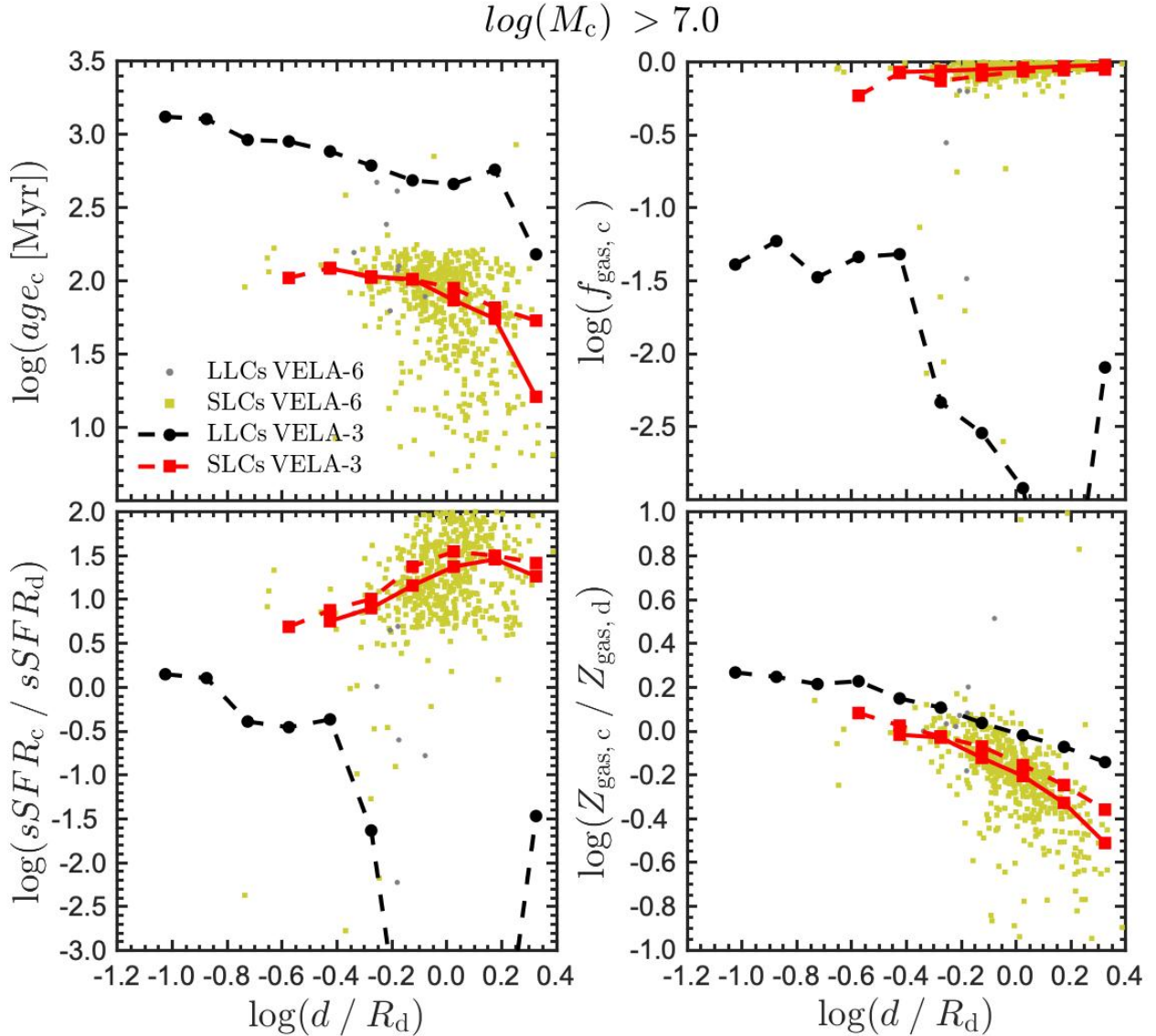


Figure 9. Gradients of clump properties with galactocentric distance for VELA-6 SLC clumps (yellow points) and LLCs (grey points). Lines represent median values for VELA-6 (solid) and VELA-3 (dash). Top-left: mass-weighted mean stellar age; Top-right: gas fraction; bottom left clump sSFR normalized to the disc sSFR; bottom-right: clump metallicity normalized to the mean disc metallicity. In-situ clumps in VELA-6 show a steep age gradient with typical clump ages of 100-200 Myr. They are gas-rich, with higher sSFR and lower metallicities than the disc.

in VELA-6. This decreases the maximum of stellar mass by a factor of 2, because of the self-regulation by feedback. This maximum of compaction happens after the central mass becomes dominated by stars in both cases. It seems that feedback weakens compaction and gas inflows within the galaxy by less than a factor of 2. After that maximum of compaction, both gas mass and SFR strongly decreases, due to gas consumption and strong outflows driven by the nuclear starburst (Z15). However, in VELA-6, the stellar mass and dark-matter mass decreases by a factor of 2, due to fluctuations in the gravitational potential induced by gas outflows (Pontzen & Governato 2012). As a result, the stellar mass after compaction in VELA-6 is 0.5 dex lower than in VELA-3.

The overall evolution of high- z galaxies in the Σ_1 -sSFR plane

is insensitive to the strength of feedback once these properties are normalized. Figure 12 shows this behaviour in the plane between $\Delta \log(\text{sSFR}) = \log(\text{sSFR}) - \log(\text{sSFR}_{\text{MS}})$ and $\Delta \log(\Sigma_1) = \log(\Sigma_1) - \log(\Sigma_{1, \text{max}})$, where $\text{sSFR}(z)_{\text{MS}}$ marks the star-forming main sequence and $\Sigma_{1, \text{max}}$ is the maximum Σ_1 value of each galaxy, as described in Z15. Galaxies in VELA-6 evolve around the main-sequence (horizontal branch in Figure 12), with slightly higher deviations than in VELA-3 (Larkin et al. in prep.) After they reach the point of maximum compaction, they evolve below the main sequence (vertical branch), initialising a process of quenching that could be completed and maintained with the aid of AGN feedback (not included in these simulations). A recent, in-depth study of wet compaction can be found in Lapiner et al. (2023).

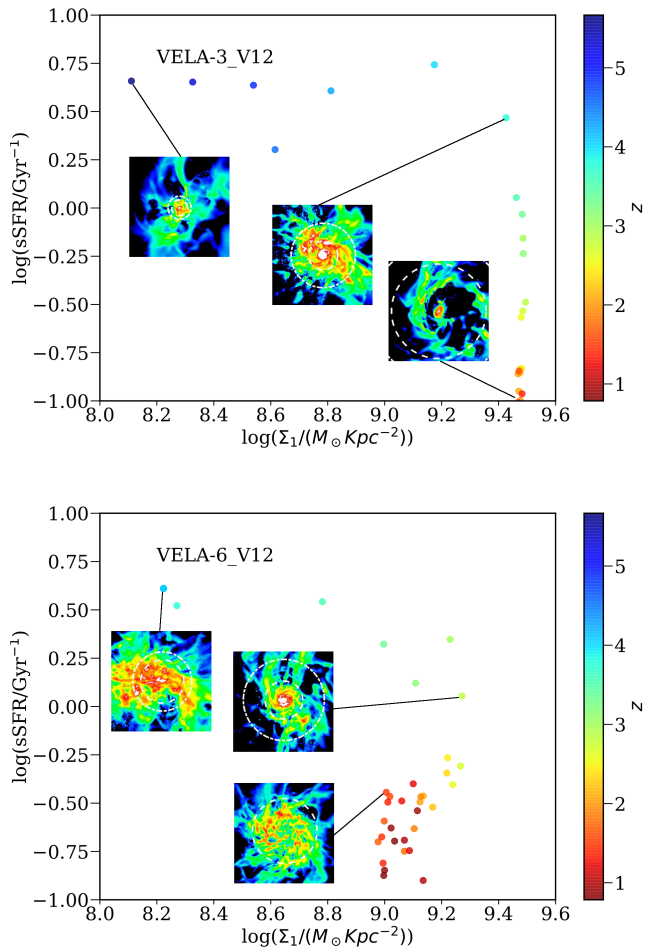


Figure 10. Example of compaction and quenching of the galaxy V12 in the VELA-3 (top) and VELA-6 (bottom) suite in the Σ_1 -sSFR plane. The maps show the gas surface density at the relevant phases: pre-compaction, compaction and post-compaction times with a scale of 10 kpc.

7 CONCLUSIONS AND DISCUSSION

We have compared two sets of cosmological, zoom-in simulations of 35 high- z galaxies with the same initial conditions but different models of stellar feedback (with and without kinetic feedback, §2.5). The model with stronger feedback (VELA-6) gives the following results with respect to the previous model (VELA-3):

- At a fixed halo mass and redshift, the galaxy stellar mass is reduced by a factor of ~ 1 -3, making the stellar-mass-halo-mass relation in better agreement with abundance matching results (Figure 1).
- In agreement with previous works (C15), the degree of 3D elongation in a galaxy is higher for lower stellar-to-DM mass ratios within the half-light radius. Low-mass galaxies, $M_* < 10^{10} M_\odot$ at $z \geq 1$, are more elongated at a fixed stellar mass in VELA-6 (Figure 2).
- The population of dense, round, compact, old ($\text{age}_c > 300$ Myr), quenched ($\log(\text{sSFR}_c/\text{sSFR}_d) < -3$), stellar (or gas poor) clumps is absent in VELA-6. Therefore, the distribution of stellar mass, traced by rest-frame near-IR bands, is significantly less clumpy than the distribution of star forming regions, traced by rest-frame UV (Figure 6).

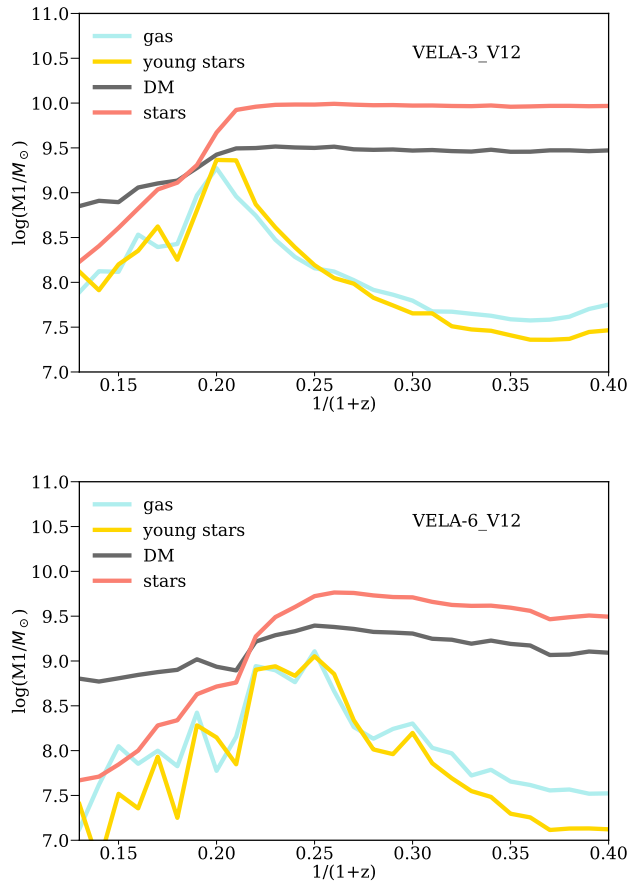


Figure 11. Evolution of the mass within 1 kpc, M_1 , of the different components of the galaxy V12 in the VELA-3 (top) and VELA-6 (bottom) suite. The increase in the central gas mass starts a compaction event, weaker by a factor 2 in VELA-6.

- Migrating clumps with clump times longer than the disc dynamical time have shorter stellar ages ($\text{age}_c = 100 - 200$ Myr) and higher baryonic densities and circular velocities (Figure 7).
- In VELA-6, the rarer long-lived clumps with lifetimes longer than 20 free-fall times are limited to the most massive clumps ($M_c/M_d \geq 0.03$) with masses similar to the Toomre mass (Figure 8).
- The evolution of compaction and quenching in the Σ_1 -sSFR plane is similar in both models (Figure 12).

Our results suggest that JWST observations will be crucial for our understanding of galaxy evolution at high- z . Rest-frame near-IR images of galaxies at cosmic noon will be able to map the stellar distribution of clumpy galaxies in great detail. JWST will also observe low-mass elongated galaxies, which should dominate the number of galaxies at high- z . The great capabilities of JWST will allow us to study these processes at even higher redshifts. For example, recent NIRCcam observations of galaxies at $z \approx 6 - 8$ have shown very clumpy morphologies (Chen et al. 2023). We expect that new observational constraints on clump properties, particularly age and mass distributions, may help distinguish between different feedback models. At the same time, the dependences of clumps on star formation models (Buck et al. 2019) may add degeneracies that complicates the interpretation of these new observations. More simulations with a wide range of models are needed.

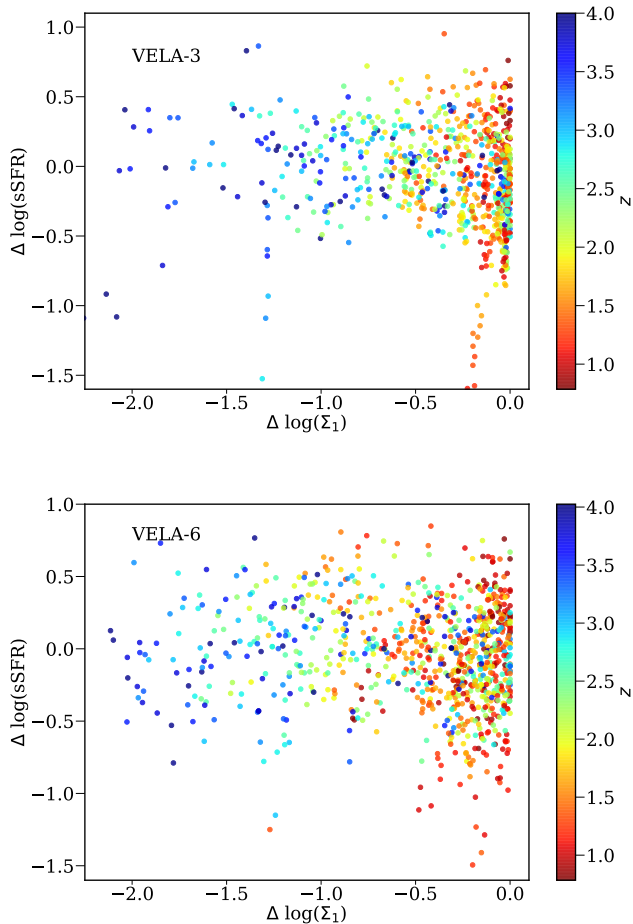


Figure 12. $\log(\text{sSFR})-\log(\text{sSFR}_{\text{MS}})$ vs $\log(\Sigma_1)-\log(\Sigma_{1,\text{max}})$ for VELA-3 (top) and VELA-6 (bottom) coloured by redshift. The galaxies in both models evolve along a universal L-shape track, first along a horizontal path, following the star-forming main sequence, and then, after compaction, along a vertical, quenching path.

The VELA project allows us to compare a large sample of zoom-in simulations performed with different models of feedback. This unique dataset provides overall trends with feedback strength. In Ceverino et al. (2014), Moody et al. (2014) and Mandelker et al. (2017), we compared the effect of feedback in the previous suites of the VELA simulations: VELA-2 (thermal-only feedback) and VELA-3 (thermal plus radiative feedback). The addition of radiative feedback reduces the gas mass in the high-values tail of the density distribution function. The galaxy stellar mass growth is therefore reduced by a factor ~ 2 . The addition of kinetic feedback reduces the stellar mass by another factor of a few. Radiative feedback also reduces the number of long-lived clumps with respect to the thermal-only case. This trend continues in VELA-6. Therefore, there is a threshold for clump disruption that increases with feedback. In VELA-2, clumps are dissolved in a few free-fall times if their baryonic column density is $\Sigma_{\text{bar}} < 100 M_{\odot} \text{pc}^{-2}$. The addition of radiative feedback in VELA-3 increases that threshold to $200 M_{\odot} \text{pc}^{-2}$. It becomes $400 M_{\odot} \text{pc}^{-2}$ with the inclusion of kinetic feedback in VELA-6. As feedback strength increases, only denser clumps can survive for a significant amount of time.

ACKNOWLEDGEMENTS

We thank the anonymous referee for comments that improve the quality of this paper. We acknowledge stimulating discussions with Guillermo Tenorio-Tagle, Sergey Silich and Casiana Muñoz-Tuñón. The VELA simulations were performed at the National Energy Research Scientific Computing Center (NERSC) at Lawrence Berkeley National Laboratory, and at NASA Advanced Supercomputing (NAS) at NASA Ames Research Center. DC is a Ramon-Cajal Researcher and is supported by the Ministerio de Ciencia, Innovación y Universidades (MICIU/FEDER) under research grant PID2021-122603NB-C21. NM acknowledges support from ISF grant 3061/21, from the Gordon and Betty Moore Foundation through Grant GBMF7392 and from the National Science Foundation under Grant No. NSF PHY-1748958. AD was partly supported by ISF 861/20.

DATA AVAILABILITY

The data underlying this article will be shared on reasonable request to the corresponding author.

REFERENCES

- Agertz O., Kravtsov A. V., 2015, *ApJ*, **804**, 18
 Agertz O., Teyssier R., Moore B., 2009, *MNRAS*, **397**, L64
 Allgood B., Flores R. A., Primack J. R., Kravtsov A. V., Wechsler R. H., Faltenbacher A., Bullock J. S., 2006, *MNRAS*, **367**, 1781
 Barro G., et al., 2013, *ApJ*, **765**, 104
 Behroozi P. S., Silk J., 2015, *ApJ*, **799**, 32
 Behroozi P. S., Wechsler R. H., Conroy C., 2013, *ApJ*, **770**, 57
 Behroozi P., Wechsler R. H., Hearin A. P., Conroy C., 2019, *MNRAS*, **488**, 3143
 Binney J., Tremaine S., 2008, *Galactic Dynamics: Second Edition*. Princeton University Press
 Birnboim Y., Dekel A., 2003, *MNRAS*, **345**, 349
 Bournaud F., Elmegreen B. G., 2009, *ApJ*, **694**, L158
 Bryan G. L., Norman M. L., 1998, *ApJ*, **495**, 80
 Buck T., Macciò A. V., Obreja A., Dutton A. A., Domínguez-Tenreiro R., Granato G. L., 2017, *MNRAS*, **468**, 3628
 Buck T., Dutton A. A., Macciò A. V., 2019, *MNRAS*, **486**, 1481
 Cattaneo A., et al., 2009, *Nature*, **460**, 213
 Ceverino D., Klypin A., 2009, *ApJ*, **695**, 292
 Ceverino D., Dekel A., Bournaud F., 2010, *MNRAS*, **404**, 2151
 Ceverino D., Klypin A., Klimek E. S., Trujillo-Gomez S., Churchill C. W., Primack J., Dekel A., 2014, *MNRAS*, **442**, 1545
 Ceverino D., Primack J., Dekel A., 2015, *MNRAS*, **453**, 408
 Ceverino D., Sánchez Almeida J., Muñoz Tuñón C., Dekel A., Elmegreen B. G., Elmegreen D. M., Primack J., 2016a, *MNRAS*, **457**, 2605
 Ceverino D., Arribas S., Colina L., Rodríguez Del Pino B., Dekel A., Primack J., 2016b, *MNRAS*, **460**, 2731
 Ceverino D., Glover S. C. O., Klessen R. S., 2017a, *MNRAS*, **470**, 2791
 Ceverino D., Glover S. C. O., Klessen R. S., 2017b, *MNRAS*, **470**, 2791
 Chen Z., Stark D. P., Endsley R., Topping M., Whittler L., Charlot S., 2023, *MNRAS*, **518**, 5607
 Costantin L., et al., 2021, *ApJ*, **913**, 125
 Croton D. J., et al., 2006, *MNRAS*, **365**, 11
 Dekel A., Burkert A., 2014, *MNRAS*, **438**, 1870
 Dekel A., Shlosman I., 1983, in Athanassoula E., ed., *IAU Symposium Vol. 100, Internal Kinematics and Dynamics of Galaxies*. p. 187
 Dekel A., Silk J., 1986, *ApJ*, **303**, 39
 Dekel A., et al., 2009a, *Nature*, **457**, 451
 Dekel A., Sari R., Ceverino D., 2009b, *ApJ*, **703**, 785
 Dekel A., Sarkar K. C., Jiang F., Bournaud F., Krumholz M. R., Ceverino D., Primack J. R., 2019, *MNRAS*, **488**, 4753

- Dekel A., Ginzburg O., Jiang F., Freundlich J., Lapiner S., Ceverino D., Primack J., 2020a, *MNRAS*, **493**, 4126
- Dekel A., et al., 2020b, *MNRAS*, **496**, 5372
- Dekel A., Tziperman O., Sarkar K., Ginzburg O., Mandelker N., Ceverino D., Primack J., 2022a, arXiv e-prints, p. arXiv:2209.04462
- Dekel A., Mandelker N., Bournaud F., Ceverino D., Guo Y., Primack J., 2022b, *MNRAS*, **511**, 316
- Elmegreen B. G., Elmegreen D. M., 2005, *ApJ*, **627**, 632
- Fabian A. C., 2012, *ARA&A*, **50**, 455
- Förster Schreiber N. M., Wuyts S., 2020, *ARA&A*, **58**, 661
- Förster Schreiber N. M., Genzel R., Bouché N., Cresci G., Davies R., Buschkamp P., Shapiro K., et al., 2009, *ApJ*, **706**, 1364
- Genel S., Dekel A., Cacciato M., 2012, *MNRAS*, **425**, 788
- Genry E. S., Krumholz M. R., Dekel A., Madau P., 2017, *MNRAS*, **465**, 2471
- Genzel R., Tacconi L. J., Eisenhauer F., Förster Schreiber N. M., Cimatti A., et al. 2006, *Nature*, **442**, 786
- Genzel R., et al., 2008, *ApJ*, **687**, 59
- Ginzburg O., Huertas-Company M., Dekel A., Mandelker N., Snyder G., Ceverino D., Primack J., 2021, *MNRAS*, **501**, 730
- Governato F., Willman B., Mayer L., Brooks A., Stinson G., Valenzuela O., Wadsley J., Quinn T., 2007, *MNRAS*, **374**, 1479
- Guo Y., et al., 2015, *ApJ*, **800**, 39
- Guo Y., et al., 2018, *ApJ*, **853**, 108
- Hopkins P. F., Quataert E., Murray N., 2012a, *MNRAS*, **421**, 3522
- Hopkins P. F., Kereš D., Murray N., Quataert E., Hernquist L., 2012b, *MNRAS*, **427**, 968
- Hopkins P. F., Kereš D., Oñorbe J., Faucher-Giguère C.-A., Quataert E., Murray N., Bullock J. S., 2014, *MNRAS*, **445**, 581
- Huertas-Company M., et al., 2020, *MNRAS*, **499**, 814
- Inoue S., Dekel A., Mandelker N., Ceverino D., Bournaud F., Primack J., 2016, *MNRAS*, **456**, 2052
- Jiang F., et al., 2019, *MNRAS*, **488**, 4801
- Jing Y. P., Suto Y., 2002, *ApJ*, **574**, 538
- Jonsson P., 2006, *MNRAS*, **372**, 2
- Jonsson P., Groves B. A., Cox T. J., 2010, *MNRAS*, **403**, 17
- Klypin A., Zhao H., Somerville R. S., 2002, *ApJ*, **573**, 597
- Kravtsov A. V., 2003, *ApJ*, **590**, L1
- Kravtsov A. V., Klypin A. A., Khokhlov A. M., 1997, *ApJS*, **111**, 73
- Kretschmer M., Dekel A., Freundlich J., Lapiner S., Ceverino D., Primack J., 2021, *MNRAS*, **503**, 5238
- Krumholz M. R., Dekel A., 2010, *MNRAS*, **406**, 112
- Langan I., Ceverino D., Finlator K., 2020, *MNRAS*, **494**, 1988
- Lapiner S., et al., 2023, arXiv e-prints, p. arXiv:2302.12234
- Law D. R., Steidel C. C., Shapley A. E., Nagy S. R., Reddy N. A., Erb D. K., 2012, *ApJ*, **745**, 85
- Leitherer C., et al., 1999, *ApJS*, **123**, 3
- Leja J., et al., 2019, *ApJ*, **877**, 140
- Madau P., Dickinson M., 2014, *ARA&A*, **52**, 415
- Mandelker N., Dekel A., Ceverino D., Tweed D., Moody C. E., Primack J., 2014, *MNRAS*, **443**, 3675
- Mandelker N., Dekel A., Ceverino D., DeGraf C., Guo Y., Primack J., 2017, *MNRAS*, **464**, 635
- Meng X., Gnedin O. Y., Li H., 2019, *MNRAS*, **486**, 1574
- Moody C. E., Guo Y., Mandelker N., Ceverino D., Mozena M., Koo D. C., Dekel A., Primack J., 2014, *MNRAS*, **444**, 1389
- Moster B. P., Naab T., White S. D. M., 2013, *MNRAS*, **428**, 3121
- Moster B. P., Naab T., White S. D. M., 2018, *MNRAS*, **477**, 1822
- Muratov A. L., Kereš D., Faucher-Giguère C.-A., Hopkins P. F., Quataert E., Murray N., 2015, *MNRAS*, **454**, 2691
- Noguchi M., 1999, *ApJ*, **514**, 77
- Oklopčić A., Hopkins P. F., Feldmann R., Kereš D., Faucher-Giguère C.-A., Murray N., 2017, *MNRAS*, **465**, 952
- Oppenheimer B. D., Davé R., 2006, *MNRAS*, **373**, 1265
- Oppenheimer B. D., Davé R., 2008, *MNRAS*, **387**, 577
- Ostriker E. C., Shetty R., 2011, *ApJ*, **731**, 41
- Pillepich A., et al., 2019, *MNRAS*, **490**, 3196
- Pontzen A., Governato F., 2012, *MNRAS*, **421**, 3464
- Roca-Fàbrega S., et al., 2019, *MNRAS*, **484**, 3625
- Rodríguez-Puebla A., Primack J. R., Avila-Reese V., Faber S. M., 2017, *MNRAS*, **470**, 651
- Schaye J., et al., 2015, *MNRAS*, **446**, 521
- Schneider M. D., Frenk C. S., Cole S., 2012, *J. Cosmology Astropart. Phys.*, **2012**, 030
- Simons R. C., et al., 2019, *ApJ*, **874**, 59
- Snyder G. F., Lotz J., Moody C., Peth M., Freeman P., Ceverino D., Primack J., Dekel A., 2015, *MNRAS*, **451**, 4290
- Stinson G., Seth A., Katz N., Wadsley J., Governato F., Quinn T., 2006, *MNRAS*, **373**, 1074
- Stinson G. S., Brook C., Macciò A. V., Wadsley J., Quinn T. R., Couchman H. M. P., 2013, *MNRAS*, **428**, 129
- Strawn C., et al., 2021, *MNRAS*, **501**, 4948
- Tacchella S., Dekel A., Carollo C. M., Ceverino D., DeGraf C., Lapiner S., Mandelker N., Primack Joel R., 2016a, *MNRAS*, **457**, 2790
- Tacchella S., Dekel A., Carollo C. M., Ceverino D., DeGraf C., Lapiner S., Mandelker N., Primack J. R., 2016b, *MNRAS*, **458**, 242
- Tacchella S., Bose S., Conroy C., Eisenstein D. J., Johnson B. D., 2018, *ApJ*, **868**, 92
- Tomassetti M., et al., 2016, *MNRAS*, **458**, 4477
- Toomre A., 1964, *ApJ*, **139**, 1217
- Vogelsberger M., et al., 2014, *MNRAS*, **444**, 1518
- Whitaker K. E., van Dokkum P. G., Brammer G., Franx M., 2012, *ApJ*, **754**, L29
- White H. A., Fisher D. B., Abraham R. G., Glazebrook K., Obreschkow D., 2022, *ApJ*, **926**, 32
- Wisnioski E., Förster Schreiber N. M., Wuyts S., Wuyts E., Bandara K., et al. 2015, *ApJ*, **799**, 209
- Wuyts S., et al., 2012, *ApJ*, **753**, 114
- Zemp M., Gnedin O. Y., Gnedin N. Y., Kravtsov A. V., 2012, *ApJ*, **748**, 54
- Zhang H., et al., 2019, *MNRAS*, **484**, 5170
- Zolotov A., et al., 2015, *MNRAS*, **450**, 2327
- van der Wel A., Chang Y.-Y., Bell E. F., Holden B. P., Ferguson H. C., et al. 2014, *ApJ*, **792**, L6

This paper has been typeset from a $\text{\TeX}/\text{\LaTeX}$ file prepared by the author.